ORIGINAL ARTICLE

gebiology   WILEY

Constraining oceanic oxygenation during the Shuram excursion in South China using thallium isotopes

Haifeng Fan[1,2] | Sune G. Nielsen[3,4] | Jeremy D. Owens[5] | Maureen Auro[3] |
Yunchao Shu[3] | Dalton S. Hardisty[6] | Tristan J. Horner[3,7] | Chelsie N. Bowman[5] |
Seth A. Young[5] | Hanjie Wen[1,2]

[1]State Key Laboratory of Ore Deposit Geochemistry, Institute of Geochemistry, Chinese Academy of Sciences, Guiyang, China

[2]University of Chinese Academy of Sciences, Beijing, China

[3]NIRVANA Laboratories, Woods Hole Oceanographic Institution, Woods Hole, MA, USA

[4]Department of Geology & Geophysics, Woods Hole Oceanographic Institution, Woods Hole, MA, USA

[5]Department of Earth, Ocean and Atmospheric Science, National High Magnetic Field Laboratory, Florida State University, Tallahassee, FL, USA

[6]Department of Earth and Environmental Sciences, Michigan State University, East Lansing, MI, USA

[7]Department of Marine Chemistry and Geochemistry, Woods Hole Oceanographic Institution, Woods Hole, MA, USA

Correspondence
Haifeng Fan, State Key Laboratory of Ore Deposit Geochemistry, Institute of Geochemistry, Chinese Academy of Sciences, Guiyang 550081, China.
Email: fanhaifeng@mail.gyig.ac.cn

Present address
Yunchao Shu, CAS Key Laboratory of Crust-Mantle Materials and Environments, School of Earth and Space Sciences, University of Science and Technology of China, Hefei, China

Abstract

Ediacaran sediments record an unusual global carbon cycle perturbation that has been linked to widespread oceanic oxygenation, the Shuram negative C isotope excursion (NCIE). However, proxy-based estimates of global ocean redox conditions during this event have been limited largely due to proxy specificity (e.g., euxinic sediments for Mo and U isotopes). Modern global seawater documents a homogenous Tl isotope composition (ε^{205}Tl = −6.0) due to significant manganese oxide burial, which is recorded in modern euxinic sediments. Here, we provide new data documenting that sediments deposited beneath reducing but a non-sulfidic water column from the Santa Barbara Basin (ε^{205}Tl = −5.6 ± 0.1) also faithfully capture global seawater Tl isotope values. Thus, the proxy utilization of Tl isotopes can extend beyond strictly euxinic settings. Second, to better constrain the global redox conditions during the Shuram NCIE, we measured Tl isotopes of locally euxinic and ferruginous shales of the upper Doushantuo Formation, South China. The ε^{205}Tl values of these shales exhibit a decreasing trend from ≈−3 to ≈−8, broadly coinciding with the onset of Shuram NCIE. There are ε^{205}Tl values (−5.1 to −7.8) during the main Shuram NCIE interval that approach values more negative than modern global seawater. These results suggest that manganese oxide burial was near or even greater than modern burial fluxes, which is likely linked to an expansion of oxic conditions. This ocean oxygenation may have been an important trigger for the Shuram NCIE and evolution of Ediacaran-type biota. Subsequently, Tl isotopes show an increasing trend from the modern ocean value to values near the modern global inputs or even heavier (ε^{205}Tl ≈ −2.5 ~ 0.4), occurring prior to recovery from the NCIE. These records may suggest that there was

a decrease in the extent of oxygenated conditions in the global oceans during the late stage of the Shuram NCIE.

KEYWORDS

Doushantuo Formation, ocean oxygenation, Shuram NCIE, thallium isotopes

1 | INTRODUCTION

The Shuram negative carbon isotope excursion (NCIE) is fundamentally different from all known carbon isotope (δ^{13}C) excursions in the geological record, with δ^{13}C decreasing from +5 to as low as −12‰, well below the mantle value of approximately −6‰ (e.g., Calver, 2000; Bristow & Kennedy, 2008; Fike, Grotzinger, Pratt, & Summons, 2006). The Shuram NCIE is documented from Ediacaran (~580–550 Ma) strata globally, although the absolute duration is uncertain with some geochronologic estimates of 10's of Myr (Le Guerroué, Allen, Cozzi, Etienne, & Fanning, 2006), while other paleomagnetic/cyclostratigraphic estimates suggest <10 Myr (Minguez, Kodama, & Hillhouse, 2015). These global observations suggest that the Shuram NCIE is a primary record of unprecedented perturbation to the global carbon cycle rather than diagenesis, and is important for understanding the coevolution of the environment and Ediacaran-type biota for this critical time interval in the latest Neoproterozoic (e.g., Fike et al., 2006; Grotzinger, Fike, & Fischer, 2011; Jiang, Kaufman, Christie-Blick, Zhang, & Wu, 2007; Kaufman, Corsetti, & Varni, 2007). Most previous studies have suggested that the Shuram NCIE may be related to a period of ocean oxygenation (e.g., Fike et al., 2006; McFadden et al., 2008), resulting in the oxidation of a massive ^{13}C-depleted dissolved organic carbon (DOC) reservoir in the deep ocean (Fike et al., 2006; Jiang et al., 2007; McFadden et al., 2008; Rothman, Hayes, & Summons, 2003). However, recent studies also suggested that local heterogeneous and transient oxygenation may have played a critical role in the expanded spatial heterogeneity of δ^{13}C and δ^{34}S excursions, not only from the Doushantuo Formation shales but also from carbonate platform regions worldwide during the Ediacaran (Li et al., 2017; Loyd et al., 2013; Osburn, Owens, Bergmann, Lyons, & Grotzinger, 2015; Shi et al., 2018). Therefore, the challenge is to establish the global extent of oceanic redox conditions for this period, which is important for understanding the connection between oceanic oxygenation and the radiation of Ediacaran-type biota because the oldest *Avalon Assemblage* occurs in a deep-water, volcaniclastic setting of the Avalon Zone of Newfoundland (Narbonne, 2005).

Thallium (Tl) isotopes have shown rapid response to changes in global marine redox conditions during the onset of associated carbon isotope excursions (Ostrander, Owens, & Nielsen, 2017; Them et al., 2018). The modern marine residence time of Tl is ~18,500 years (Baker, Rehkämper, Hinkley, Nielsen, & Toutain, 2009; Nielsen, Rehkämper, & Prytulak, 2017; Rehkämper & Nielsen, 2004), significantly longer than the ocean mixing time of ~1,500 years, thereby yielding a globally homogenous Tl isotope composition (ε^{205}Tl = 10,000 × ($^{205/203}$Tl$_{sample}$-$^{205/203}$Tl$_{SRM}$ $_{997}$)/$^{205/203}$Tl$_{SRM\,997}$) for oxic seawater of ε^{205}Tl = −6.0 ± 0.3 (Owens, Nielsen, Horner, Ostrander, & Peterson, 2017, and references therein) with concentrations of 65 ± 5 p.m. (Owens et al., 2017; Rehkämper & Nielsen, 2004). Sources of Tl to the ocean are dust aerosols, rivers, hydrothermal fluids, continental margin sediment pore fluids, and volcanic fumaroles, which are all characterized by relatively similar Tl isotope compositions of ε^{205}Tl = −2 (Baker et al., 2009; Nielsen et al., 2005, 2006, 2011, 2017). These sources are balanced by adsorption onto manganese (Mn) oxides and incorporation into oceanic crust during low-temperature hydrothermal alteration (Nielsen et al., 2006). The adsorption of Tl to Mn oxides is associated with a large positive isotope fractionation (modern ε^{205}Tl values of Mn oxides are +6 to +12; Rehkämper et al., 2002; Rehkämper, Frank, Hein, & Halliday, 2004; Nielsen et al., 2013), accounting for the burial of ~32% of the global oceanic Tl inventory. In contrast, Tl deposition within altered oceanic crust imparts a relatively minor isotope fractionation from seawater (modern ε^{205}Tl values of altered oceanic crusts are −10 to −6; Nielsen et al., 2006), constituting the majority of the remaining ~68% of the burial. There are additional sinks, but they are relatively minor and/or have limited known isotopic effect on seawater (Owens et al., 2017). Thus, the burial of Mn oxides is the most dominant flux that drives seawater Tl isotope variability, especially over shorter timescales (Owens, 2019; Owens et al., 2017). Manganese oxides are ubiquitous in oxic marine sediments deposited below an oxygenated water column but are absent under anoxic conditions including euxinic (anoxic and sulfidic water column) conditions at or above the sediment–water interface (Johnson, Webb, Ma, & Fischer, 2016; Rue, Smith, Cutter, & Bruland, 1997). Hence, the Tl isotope composition of seawater can be related to the extent of oxic conditions at the seafloor by means of the global Mn oxide burial flux (Bowman et al., 2019; Ostrander et al., 2019, 2017; Owens, 2019; Owens et al., 2017; Them et al., 2018).

Modern euxinic sediments from the Black Sea and Cariaco Basin preserve the Tl isotope signal of the overlying oxic portion of the water column (Owens et al., 2017). As such, the Tl isotope composition of ancient sediments with independent evidence for euxinic deposition can be used to reconstruct the Tl isotope composition of ancient seawater. Ostrander et al. (2017) have shown that ancient euxinic sediments from two ocean basins recorded a significant positive Tl isotope excursion prior to the Cretaceous Oceanic Anoxic Event 2 (OAE2; 94 Ma), which suggests an expansion of anoxia prior to massive organic carbon burial event. Additionally, Tl isotopes have shown a positive shift before the classically defined Toarcian OAE (T-OAE; 183 Ma), reflecting a two-step deoxygenation event (Them et al., 2018). In the

Precambrian, Tl and molybdenum isotopes were paired to document basinal or global oxygenation, which drove manganese oxide burial prior to the Great Oxidation Event (Ostrander et al., 2019). Thus, Tl isotopes record global perturbations to the burial flux of Mn oxides, which is related to the extent of oxic bottom waters and dissolved Mn availability in the ocean.

In an effort to estimate relative changes in oceanic oxygenation during the Shuram NCIE, shales in the Doushantuo Formation from four sections (spanning inner shelf to slope settings) in South China were investigated for their Tl isotope composition. We provide independent evidence from Fe speciation and redox-sensitive elements for the local paleoredox conditions of the overlying water column during deposition. To investigate the potential of low oxygen, but non-euxinic settings to record seawater Tl isotope signatures, it was first necessary to calibrate the Tl isotope proxy in a modern low oxygen setting, the Santa Barbara Basin, California, USA.

## 2 | GEOLOGICAL SETTING AND SAMPLES

2.1 | Santa Barbara Basin

A 2.8-m giant gravity sediment core was taken from the deepest portion (594 m water depth) of the Santa Barbara Basin (N 34°13′34.2″, W 120°1′49.2″) in 2001 on the R/V New Horizon. This basin, silled at 475 m, has been extensively studied due to the low bottom water oxygen concentrations occurring below the sill, typically <0.1 ml/L but can vary on seasonal timescales (Moffitt, Hill, Ohkushi, Kennett, & Behl, 2014; Reimers, Ruttenberg, Canfield, Christiansen, & Martin,

1996; Sholkovitz, 1973). The sedimentation rate in this basin is generally high, where ~2,000 years is represented by 200 cm (Reimers, Lange, Tabak, & Bernhard, 1990; Schimmelmann, Hendy, Dunn, Pak, & Lange, 2013). Generally, sediments in the basin are characterized by elevated organic carbon contents (~3–4 wt%; Raven, Sessions, Fischer, & Adkins, 2016; Schimmelmann & Kastner, 1993) with minor sulfide accumulation in the upper portion of the deep basin pore fluids (Raven et al., 2016).

2.2 | Overview of the Doushantuo Formation

The Doushantuo Formation of the Nanhua Basin in South China has zircon U-Pb ages of 635.2 ± 0.6 Ma to 551.1 ± 0.7 Ma (Condon et al., 2005). The Doushantuo Formation is underlain by the glacial diamictites of the Nantuo Formation and overlain by dolostones of the Dengying Formation (Jiang et al., 2007). Local correlations between different exposures of the Doushantuo Formation, as well as paleobasinal reconstructions, have been established based on biostratigraphy, δ^{13}C chemostratigraphic data, and U-Pb ages (e.g., Condon et al., 2005; Jiang, Shi, Zhang, Wang, & Xiao, 2011; Li et al., 2017; Liu et al., 2014; Zhu et al., 2013). For this investigation, three sections were collected from the Yangtze Gorges area, where it has been proposed that the Doushantuo Formation was deposited below wave base, in an inner shelf lagoon (Western Hubei Platform; Figure 1; Jiang et al., 2011; McFadden et al., 2008). The slope sample materials were collected from a section (Wuhe) deposited on the slope (Guizhou) of the Yangtze platform that has been interpreted as well connected with the open ocean during the Ediacaran (Figure 1; Jiang, Sohl, & Christie-Blick, 2003; Zhang et al., 2013; Zhu et al., 2013).

FIGURE 1 The simplified paleogeographic reconstruction for the Yangtze platform during deposition of the Doushantuo Formation, South China, modified from Jiang et al. (2011). There are three depositional facies in the Nanhua Basin, including the shallow shelf, slope, and basinal facies. The locations of the four sections investigated in this study marked as circled numbers. Three sections (① Baiguoyuan, ② Jiulongwan, and ③ Chenjiayuanzi) were collected from the inner and intrashelf locations in the Yangtze Gorges area. There was no barrier separating the shelf area from the open ocean (Zhu et al., 2013). One section (④ Wuhe) represents deposition on the slope that was well connected with the open ocean at that time (Jiang et al., 2003; Zhang et al., 2013)
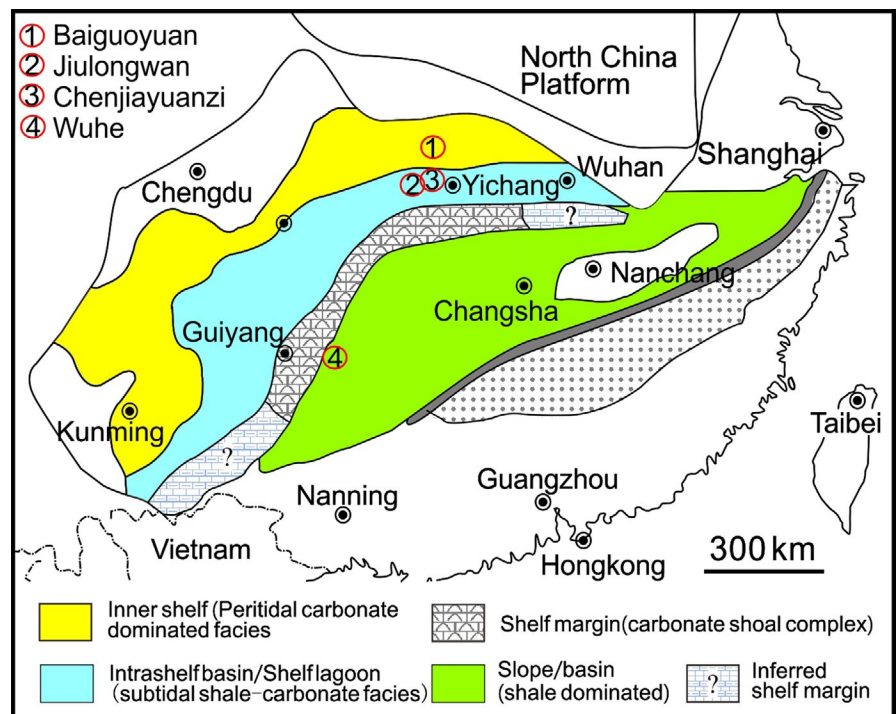
2.2.1 | The Yangtze Gorges area

The Doushantuo Formation can be generally subdivided into four members in the Yangtze Gorges area. The upper portion of the Doushantuo Formation is marked by an NCIE (Figure 2), which has been referred to as the Doushantuo negative carbon isotope excursion (DOUNCE) (Zhu et al., 2013), and is correlated with the global Shuram NCIE (Li et al., 2017). Hereafter, we refer to the DOUNCE as the Shuram NCIE. The Shuram NCIE in the Yangtze Gorges area is characterized by three distinct subdivisions, named as EN3a (onset of negative excursion), EN3b (peak of negative carbon isotope), and EN3c (a recovery to positive values) (Li et al., 2017; McFadden et al., 2008; Figure 2).

At the Baiguoyuan section (BGY, N31°19′31″, E111°03′33″), the Shuram NCIE begins at the upper part of Member III of the Doushantuo Formation and ends within the top portion of Member IV (Figure 2a; Zhu et al., 2013). In the upper part of this section, there is a ~20-m-thick black shale that has been separated into two intervals (Li et al., 2014; Tang, Ding, Yao, & Gong, 2013). The first, lower interval consists largely of laminated black shale with interbedded thin, muddy dolostone. The upper part is characterized by organic-rich black shale and dark gray mudstone (Li et al., 2014; Tang et al., 2013). Sampling locations of black shales span the EN3b and EN3c stratigraphic intervals, whereas the EN3a stratigraphic level is only scarcely present as shale (Figure 2a).

The Jiulongwan section (JLW, N30°48′54″, E111°03′20″) and the Chenjiayuanzi section (CJYZ, N30°49′50″, E111°06′31″) are located in the southern limb of the Huangling Anticline. The detailed stratigraphy and carbon isotope curves have been previously published (e.g., Jiang et al., 2007; Li et al., 2010, 2017; Liu et al., 2014; McFadden et al., 2008). The Shuram NCIE is located in the upper part of Member III to Member IV (102–155 m) of the Jiulongwan section (Figure 2b). In the Chenjiayuanzi section, the Shuram NCIE is located in the upper Member III through Member IV, ~150–183 m (Figure 2c). In these two sections, black shales

were collected from the EN3c interval. For the described black shales, Member IV of Jiulongwan section has been investigated previously for paleoredox conditions of the overlying water column, with Mo concentration and Fe speciation proxy evidence for euxinic water column conditions during deposition of this member of the Doushantuo Formation (e.g., Kendall et al., 2015; Li et al., 2010; Och et al., 2015).

2.2.2 | The Wuhe section

The Wuhe section (WH, N26°45′93.6″, E108°25′0.5″) in Guizhou Province outcrops along the Qingshui River in Taijiang County. Here, the Doushantuo Formation has also been subdivided into four members to correlate with the Yangtze Gorges area (Sahoo et al., 2016). The Wuhe carbon isotope curve is difficult to correlate with sections investigated from the Yangtze Gorges area, as the magnitude of the Wuhe negative CIE is muted (Jiang et al., 2011). Nevertheless, Sahoo et al. (2016) proposed a potential correlation between the Wuhe section and the Jiulongwan section, which indicates that the Shuram NCIE might also start at the middle/upper part of Member III. The recognition of EN3a and EN3b intervals has been difficult to constrain due to the predominance of black shales in this section that are not conducive for carbonate C isotope analyses. Here, we use new C isotope data to re-assess the approximate stratigraphic locations of EN3a and EN3b (Figure 2d, Appendix S1). These data suggest that EN3a commences in the middle of Member III, which could be consistent with C isotope data from the Jiulongwan section (McFadden et al., 2008). Black shale samples studied here were collected from Members III and IV. Previous paleoredox proxy evidence from Mo and U concentrations and Fe speciation indicate ferruginous to euxinic water column conditions during deposition of Members III and IV (Han & Fan, 2015; Sahoo et al., 2016).
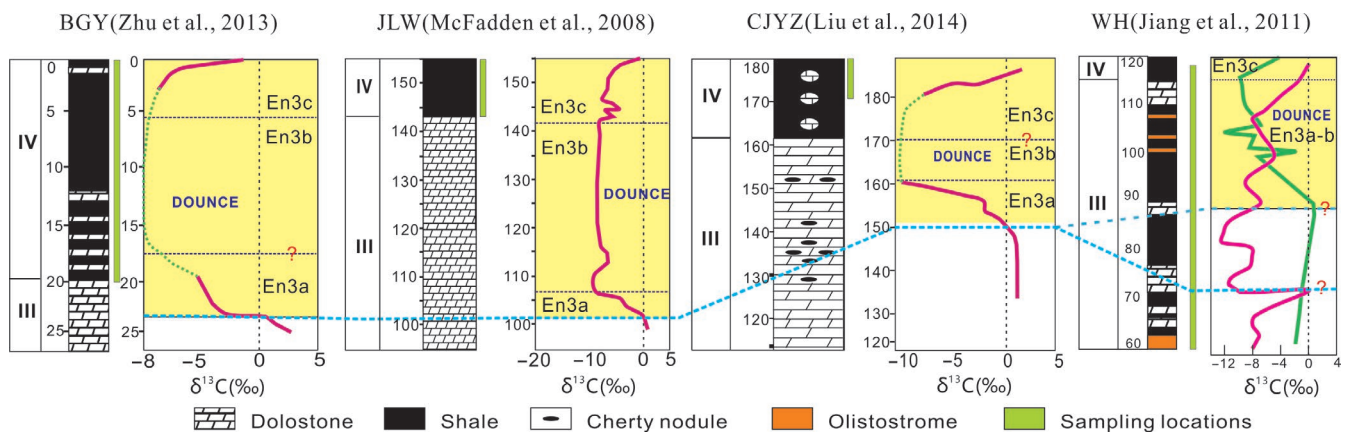

FIGURE 2 A pronounced negative carbonate carbon isotope excursion occurs in Members III through IV of the Doushantuo Formation in all studied sections, this carbon isotope excursion has been correlated with the Shuram NCIE. The potential stratigraphic correlation between three sections located in the Yangtze Gorges area and the slope section (Wuhe) follows previous studies (purple line; Jiang et al., 2007; Jiang et al., 2011; Sahoo et al., 2016) and our new data (green line, Table A1). The green bars indicate interval sampled in this study. The green line in the Wuhe section represents carbon isotope curve in this study (Appendix S1). BGY, Baiguoyuan; CJYZ, Chenjiayuanzi; JLW, Jiulongwan; WH, Wuhe

3 | METHODS

3.1 | Authigenic Tl isotope and concentration analysis

The modern Santa Barbara samples were dissolved and analyzed in a trace metal-free clean laboratory in the Geochemistry group at the National High Magnetic Field Laboratory (NHMFL), Florida State University. Approximately 100 mg of dried and powdered samples was digested in polytetrafluoroethylene (PTFE) beakers using 3 ml of 2 M HNO_3 at 130°C for 12 hr. The supernatant solution was centrifuged and completely evaporated, and then redissolved in a CEM Mars 5 microwave for 2 hr to completely digest all residual organic matter.

The concentration and isotopic composition of authigenic Tl in ancient shales were measured following a partial dissolution method (modified after Owens et al., 2017) that was performed in a class 100 metal-free clean laboratory at the NIRVANA Laboratories, Woods Hole Oceanographic Institution (WHOI). Approximately 200 mg of powdered samples was digested in PTFE beakers using 10 ml concentrated HNO_3 at 135°C for 12 hr. The supernatant, which is considered to contain primarily authigenic Tl that may be bound to sulfides (Nielsen et al., 2011; Owens et al., 2017), was separated from the residual solids by centrifugation and complete evaporation. The samples were then redissolved in 3 ml concentrated HNO_3 and transferred into 90-ml quartz glass vials. The 90-ml vials were sealed with PTFE thread seal tape and heated to 260°C at 110 bars of pressure for 1.5 hr in an Anton Parr high-pressure asher (HPA). Each sample was subjected to the HPA procedure twice to ensure complete digestion of any residual organic matter that may interfere with the chemical separation of Tl from sample matrix. After digestion in the HPA, a 10% aliquot was used for chemical purification of Tl.

All Tl was separated from the sample matrix using a single PTFE mini-column containing 0.1 ml (AG1-X8 resin; Ostrander et al., 2017). Thallium isotope ratios and concentrations were measured using a Neptune multi-collector inductively coupled plasma mass spectrometer (MC-ICP-MS) at the WHOI Plasma Facility or NHMFL. Each sample required the addition of NIST SRM981 Pb with standard-sample bracketing applied for instrumental mass bias correction to determine the Tl isotope ratio (Nielsen, Rehkämper, Baker, & Halliday, 2004). Thallium concentrations were calculated by monitoring $^{205}Tl/^{208}Pb$ ratios during isotopic measurements because a known quantity of NIST SRM981 Pb was added to each sample. Thallium isotopic compositions are reported relative to the NIST SRM 997 Tl solution, $\varepsilon^{205}Tl = 10,000 \times (^{205/203}Tl_{sample} - {}^{205/203}Tl_{SRM\,997})/{}^{205/203}Tl_{SRM\,997}$.

Application of the two different acid strengths used in the two different laboratories for extracting the authigenic Tl component has been shown to result in identical Tl isotope compositions for the USGS reference material SCo-1 (Bowman et al., 2019; Ostrander et al., 2019, 2017; Owens et al., 2017; Them et al., 2018). Here, we also evaluate the entire chemical separation procedure by analyzing the USGS reference material SCo-1 (shale) six times to monitor external precision and accuracy. The average $\varepsilon^{205}Tl$ value

of SCo-1 was determined as $\varepsilon^{205}Tl = -2.8 \pm 0.3$ (2sd, $n = 6$), in excellent agreement with previous studies that obtained $\varepsilon^{205}Tl = -2.9$ to -3.0 (Bowman et al., 2019; Ostrander et al., 2019, 2017; Owens et al., 2017; Them et al., 2018). Based on the measurements of SCo-1, we estimate the long-term external reproducibility to be ≈0.3 $\varepsilon^{205}Tl$(2sd) and apply this error as a minimum to all sample analyses unless the repeated sample measurement was greater than this error.

3.2 | Major and trace element concentrations of bulk rocks

Elemental compositions for the Santa Barbara Basin samples utilized a standard multi-acid digestion that used trace metal clean HNO_3, HCl, and HF. Sample masses of approximately 100 mg were weighed into PTFE beakers and microwave-digested using a CEM MARS 5 to remove organic carbon without volatilizing redox-sensitive trace elements. Further treatment with nitric and hydrochloric acid at different temperatures on a hotplate was used to completely dissolve the samples. After complete dissolution of the samples, they were dried down and dissolved in 2% HNO_3 for analysis on an Agilent 7500cs quadrupole inductively coupled plasma mass spectrometer (ICP-MS) for trace metal concentrations at the NHMFL at FSU. Blank concentrations were below detection limits, and replicate analyses of USGS standard SDO-1 were within <5% of the reported values for all elements.

For the major element analyses of shale samples in the Doushantuo Formation, powdered samples were mixed with a lithium tetraborate powder in a platinum crucible. The mixture was melted and formed into pellets, which underwent high-temperature (>1,000°C) glass fusion for 2 hr. The major elements (Al, Fe, and Mn) were determined using X-ray fluorescence (XRF) at the ALS Chemex (Guangzhou) Co., Ltd. Trace element (Tl, Mo, U) concentrations of bulk rocks were measured at the Institute of Geochemistry (Guiyang), Chinese Academy of Sciences. Powder samples (50 mg) were digested in a PTFE bomb using ultrapure HF and HNO_3 acids under pressure at high temperature (190°C) for 12 hr. After complete digestion and acid evaporation, the samples were diluted in 3% HNO_3 with Rh internal standard solution. This solution was analyzed for trace elements using an ICP-MS. During the analytical processes, a standard reference material SBC-1 was measured alongside samples and gave elemental concentrations consistent with certified values (Table 1). The calculation of Mo and U enrichment factors (Mo_{EF} and U_{EF}) and $(Mo/U)_{Auth}$ followed methods outlined in Tribovillard, Algeo, Lyons, and Riboulleau (2006) and Algeo and Tribovillard (2009). The uncertainty on Mo_{EF} and U_{EF} is dependent on that of the Mo, U, and Al concentrations.

3.3 | Fe speciation sequential extraction

We used the method outlined by Poulton and Canfield (2005) that has been widely adopted for the sequential extraction of reactive

iron species (Appendix S1). Using approximately 100 mg of powdered sample, the sequential extraction is as follows: (a) Fe associated with carbonate phases (Fe_{carb}) including siderite and ankerite was extracted using sodium acetate; (b) Fe associated with crystalline oxide phases (Fe_{oxide}) including goethite and hematite was extracted by sodium dithionite; and (c) Fe in magnetite (Fe_{mag}) was extracted using ammonium oxalate. After each extraction, an aliquot of the solution was analyzed on an Agilent 7500cs quadrupole ICP-MS at the NHMFL. The Fe_{py} concentrations were determined by the gravimetric yields of extracted Ag_2S from samples using the chromium reducible sulfide extraction method modified from Canfield, Raiswell, Westrich, Reaves, and Berner (1986) in the Young Lab at FSU, and assuming a stoichiometry of FeS_2. Highly reactive Fe (Fe_{HR})-to-total Fe (Fe_T) ratio was calculated as the sum of these four species: Fe_{carb}, Fe_{oxide}, Fe_{mag}, and Fe_{py}.

4 | RESULTS

4.1 | Modern sediments

All data are listed in Table 1 and presented in Figures 3 and 4. The Fe_{HR}/Fe_T ratios of the Santa Barbara Basin sediments are between 0.41 and 0.46 with nearly homogenous Fe_{Py}/Fe_{HR} values as well (0.52–0.59) (Figure 3a). The Mo_{EF} is primarily between 4 and 6, and U_{EF} is not >1 (Figure 3b). Additionally, the Mn concentrations (311–353 ppm) for all of the samples are all well below the oxic to anoxic threshold of 850 ppm (Turgeon & Brumsack, 2006, and references therein). The four modern down-core sediments from the Santa Barbara Basin exhibit homogenous Tl isotope compositions, with an average of $\varepsilon^{205}Tl = -5.6 \pm 0.1$ for these samples (Table 1).

4.2 | Ediacaran organic-rich shales

The Fe_{HR}/Fe_T ratios of the Baiguoyuan samples vary from 0.28 to 0.66 (Figure 3a). The Fe_{Py}/Fe_{HR} ratios are near zero, mostly between 0.01 and 0.09. The molybdenum enrichment factors (Mo_{EF}) are between 3 and 60, with a mean of 34 (Figure 3b). Uranium enrichment factors (U_{EF}) have a narrow range from 3 to 10 with a mean value of 6. The Chenjiayuanzi and Wuhe samples show similar Fe_{HR}/Fe_T values, ranging from 0.30 to 0.63, and low Fe_{Py}/Fe_{HR} ratios, with a range of 0.01 to 0.12, with one notably high value of 0.66 in the Wuhe section (Figure 3a). For the Chenjiayuanzi samples, Mo_{EF} and U_{EF} exhibit a wide range from 28 to 192 and 4 to 31, respectively (Figure 3b). In the Wuhe section, three samples document lower Mo_{EF} and U_{EF} than 3, while the rest of the samples have uniform U_{EF} (5–10) and a wide range of Mo_{EF} (11–403) (Figure 3b). In contrast, most shales from the Jiulongwan section exhibit elevated Fe_{HR}/Fe_T ratios (0.26 to 1.0) and Fe_{Py}/Fe_{HR} values (0.71 to 0.94), except one sample (JLW-07) (Figure 3a), which is consistent with previously published work (Li et al., 2010). These samples yield high Mo_{EF} ranging from 85 to 398, compared to U_{EF} from 4 to 16. These values are

similar to previous studies that have also reported high Mo enrichments for the Doushantuo Formation (Han & Fan, 2015; Kendall et al., 2015; Och et al., 2015).

The overall variation of Tl isotope composition in all investigated Doushantuo shales is between $\varepsilon^{205}Tl = -7.8$ at the Wuhe section and $\varepsilon^{205}Tl = +0.4$ at the Baiguoyuan section (Figure 4). The only portion of the Shuram NCIE that is represented in all four sections is EN3c, with values clustered around $\varepsilon^{205}Tl \approx -2.5$ to 0.4, with a few more negative values toward the very top of EN3c (Figure 4). Only the Baiguoyuan and Wuhe sections contain samples from EN3a and EN3b, and Wuhe only contains three samples from these intervals (Figure 4), such that direct correlations of Tl isotopes between these two sections are not possible. The EN3a portion of Baiguoyuan suggests a gradual decrease in Tl isotope values from $\varepsilon^{205}Tl \approx -3.1$ to −4.8, whereas samples from EN3b at the Baiguoyuan section generally display values of $\varepsilon^{205}Tl \approx -6.5$ to −4.2. The three samples from EN3a and EN3b at Wuhe are in general agreement with these values at $\varepsilon^{205}Tl \approx -7.8$ to −5.1.

5 | DISCUSSION

5.1 | Proxy calibration at Santa Barbara Basin

The ratios of Fe_{HR}/Fe_T in sediments deposited from oxic water columns are usually at or below 0.38, with a modern average of 0.26 ± 0.08 and a Phanerozoic average (past 542 Myr, excluding the modern) of 0.14 ± 0.08 (Lyons & Severmann, 2006; Poulton & Raiswell, 2002; Raiswell & Canfield, 1998; Raiswell et al., 2018). However, this ratio usually exceeds 0.38 for sediments deposited under an anoxic water column, which arises from excess Fe delivery relative to typical detrital input and the preservation of Fe(II) minerals (e.g., Poulton & Raiswell, 2002; Raiswell & Canfield, 1998). Excess Fe is primarily delivered to these environments via diffusion of soluble Fe(II) from reductive dissolution of Fe oxides along the continental shelf, elevating the Fe_{HR} pool through an "Fe shuttle" to deeper basinal settings where it is captured as syngenetic pyrite (e.g., Lyons & Severmann, 2006; Raiswell & Canfield, 1998). When Fe_{HR}/Fe_T exceeds 0.38, the Fe_{Py}/Fe_{HR} ratios of sediments deposited under euxinic conditions are >0.70, indicating Fe-limited pyrite formation and, thus, excess hydrogen sulfide from microbial sulfate reduction due to organic carbon decomposition(März et al., 2008; Poulton & Canfield, 2011). When anoxic conditions are indicated by $Fe_{HR}/Fe_T > 0.38$, but Fe_{Py}/Fe_{HR} values are <0.7, it is interpreted to be deposited under ferruginous conditions, reflecting excess Fe(II) relative to dissolved hydrogen sulfide in the water column (Berner, 1982; Poulton & Canfield, 2011).

The Fe speciation analysis of the Santa Barbara Basin sediments reveals Fe_{HR}/Fe_T of 0.41–0.46 and Fe_{Py}/Fe_{HR} of 0.52–0.59 (Figure 3a), which supports a locally reducing water column with sulfide accumulation limited to reducing pore fluids. This is consistent with some previous observations (Raven et al., 2016), but we note that the original work demonstrating Fe_{HR}/Fe_T variations

TABLE 1 Tl isotope composition and Tl concentration, Fe species data, and trace elements of the investigated samples

Sample ID	Depth m	ε^{205} Tl authigenic	2SD	Authigenic Tl ppm	Total Tl ppm	Al wt%	Fe_T wt%	Mn ppm	Mo ppm	U ppm
Baiguoyuan			N = 3							
AQH-02	0	0.0	0.3	0.69	0.96	6.58	1.21	28	35.8	14.8
AQH-03	0.5	0.2	0.1	0.73	1.05	6.94	0.63	63	36.0	8.8
AQH-04	1	−1.6	0.1	0.87	1.22	7.31	1.49	55	21.5	16.1
AQH-05	1.5	0.4	0.6	0.72	0.98	6.85	0.89	41	46.1	22.9
AQH-06	2.5	−1.0	0.3	0.77	1.06	7.04	0.89	37	47.0	22.8
AQH-07	3.5	−1.0	0.2	0.70	0.90	6.75	0.88	40	27.9	17.7
AQH-07 (duplicate)		−0.8	0.1	0.66	0.90					
AQH-08	4.5	−1.4	0.3	0.69	0.96	6.93	0.85	31	31.9	19.4
AQH-09	5.5	−6.5	0.1	1.15	1.24	7.25	3.34	57	31.6	18.1
AQH-10	6.5	−4.2	0.3	1.20	1.58	7.60	1.97	33	49.5	17.7
AQH-11	7.5	−2.8	0.5	0.87	2.04	7.94	2.16	33	42.8	15.6
AQH-12	8.5	−2.7	0.4	0.47	2.15	8.01	2.13	41	28.1	16.2
AQH-13	9.5	−6.4	0.1	2.21	2.54	7.50	2.11	33	53.3	26.7
AQH-15	11.5	−4.8	0.2	1.53	1.99	7.69	1.39	35	22.9	15.6
AQH-16	13	−6.2	0.3	1.41	1.68	7.65	1.91	34	14.7	16.2
AQH-17	14.5	−4.8	0.2	1.68	2.24	8.10	2.22	40	14.0	17.8
AQH-18	16	−3.9	0.3	1.49	1.77	8.15	1.35	29	9.3	14.0
AQH-19	17.5	−4.7	0.2	1.48	2.02	7.70	1.86	38	19.4	17.3
AQH-24	19	−3.1	0.3	1.52	1.72	6.66	2.19	98	2.7	16.0
Jiulongwan			N = 3							
JLW-03[a]	154.5	−2.5	0.3	1.71	1.98	5.29	3.33	227	118.0	30.3
JLW-06[a]	153	−1.5	0.1	1.17	1.24	4.16	2.08	303	98.5	13.2
JLW-07[a]	152.5	−1.7	0.2	0.71	0.94	5.82	2.70	152	72.3	15.8
JLW-08[a]	151.8	−1.9	0.3	0.91	1.18	4.47	2.25	227	90.8	13.8
JLW-09[a]	150.5	−1.2	0.6	1.31	1.50	5.72	2.73	152	73.0	14.3
JLW-10[a]	150	−1.2	0.1	1.41	1.55	4.86	2.32	227	127.0	16.3
JLW-11[a]	149.5	−1.6	0.9	1.75	1.92	5.56	2.83	227	133.0	17.6
JLW-12[a]	149	−2.5	0.3	1.17	1.33	5.82	2.95	152	63.6	15.2
JLW-13[a]	148	−2.4	0.3	1.35	1.41	5.10	2.37	152	89.4	7.7
JLW-14[a]	146	−0.7	0.1	1.00	1.18	5.09	2.33	227	71.8	14.9
JLW-15[a]	144	−1.4	0.4	1.60	1.84	6.14	2.84	152	291.0	13.3
JLW-16[a]	142	−0.4	0.1	1.43	1.79	6.46	3.03	227	65.2	16.8
Chenjiayuanzi			N = 3							
CJYZ-01	180	−3.0	0.8	0.24	0.60	4.76	2.94	311	61.2	22.1
CJYZ-03	179	−4.5	0.6	0.13	0.27	0.39	0.22	43	7.0	4.4
CJYZ-05	175.5	−0.7	0.3	0.92	1.12	5.79	2.82	86	86.5	15.8
CJYZ-06	174.5	−0.6	0.1	0.88	1.05	5.73	2.75	95	131.0	8.9
CJYZ-07	172.5	0.1	0.1	0.95	1.09	6.76	1.32	34	39.5	10.6
CJYZ-08	171.5	0.4	0.2	0.93	1.10	6.40	1.68	30	92.5	17.1
CJYZ-09	170	−0.1	0.4	1.03	1.19	6.58	1.15	35	21.8	16.2
Wuhe			N = 3							
WH14-14	116.8	−3.0	0.3	0.46	0.57	5.85	3.01	51	74.6	14.9
WH14-05	115.4	−1.0	0.4	0.74	0.95	8.06	3.17	35	69.1	13.7

Sample ID	Depth m	ε^{205}Tl authigenic	2SD	Authigenic Tl ppm	Total Tl ppm	Al wt%	Fe$_T$ wt%	Mn ppm	Mo ppm	U ppm
WH14-04	115.3	0.0	0.1	1.34	1.58	8.23	2.28	42	366.0	16.4
WH14-03	115.2	−0.6	0.5	1.27	1.50	8.11	2.75	64	84.4	17.1
WH14-02	115.1	0.1	0.5	1.44	1.41	8.33	2.21	25	400.0	18.3
WH14-01	115	−0.4	0.2	1.03	1.19	8.39	3.16	82	104.5	15.0
WH82[a]	104.4	−7.8	0.5	0.19	0.28	5.30	3.32	29	7.0	16.5
WH76[a]	99.1	−5.1	0.7	0.14	0.24	6.49	3.65	146	2.4	3.7
WH68[a]	88.2	−6.3	0.3	0.24	0.38	6.38	2.94	130	2.0	3.2
WH58[a]	74.5	−3.4	0.6	0.14	0.25	7.12	1.59	23	2.5	3.3
WH43[a]	56.0			0.39	0.53	5.51	2.69	57	32.9	20.2
WH42[a]	55.3	−1.2	0.4	0.43	0.57	5.86	2.91	49	69.9	16.5
Santa Barbara Basin	cm		N = 3	ppm	ppm					
NH01 12-18 G6C-47 0–1 cm	0.5	−5.5	0.1	0.74	0.56	8.59	4.51	311	4.8	2.7
NH01 12-18 G6C-47 1–2 cm	1.5	−5.6	0.2	0.41	0.54	8.77	4.54	322	5.6	2.7
NH01 12-18 G6C-47 2–3 cm	2.5	−5.7	0.2	0.38	0.58	9.50	4.77	352	6.7	2.9
NH01 12-18 G6C-47 3–4 cm	3.5	−5.7	0.1	0.42	0.54	9.59	4.73	353	4.6	2.7
Standard			N = 6	ppm	ppm					
SCo-1		−2.8	0.3	0.53	0.71					
Reference value (Ostrander et al., 2017)		−2.9	0.1							
SBC-1					0.96	11.00	6.54	1,100	2.2	6.2
Reference value[b]					0.89	11.12	6.79	1,161	2.4	5.8

Note: "−" Below detection limit. For Fe species data: A standard is used in which our reproducibility is ~7% for each extraction.

[a]Al, Fe, Mo, and U data are referenced from Han and Fan (2015).

[b]The reference value is cited from USGS.

in sediments under fluctuating water column redox states measured two sediment samples between 1 and 5 cm depth from the "dysaerobic" Santa Barbara Basin, with values of $Fe_{HR}/Fe_T < 0.25$ (Fe_{HR} only includes dithionite, pyrite, and monosulfide bound Fe; Raiswell & Canfield, 1998). The discrepancy with our data is likely due to differences in the methods as the original sequential Fe extraction scheme did not include Fe contents from Fe_{carb} and Fe_{mag} fraction. If we remove these two extractions, our data are slightly higher (average of 0.32 for upper 4 cm samples) than previously reported values but within the methodological uncertainty. We utilize the entire extraction scheme as values for Fe_{carb} and Fe_{mag} are pivotal for recognizing anoxic, ferruginous settings where pyrite is less abundant than in euxinic settings (Poulton & Canfield, 2011; Raiswell et al., 2018). Our Fe_{HR}/Fe_T data are also within analytical uncertainty of a recent study on the Santa Barbara Basin with the core top value of 0.38, but their Fe_{py}/Fe_{HR} values of 0.10 are significantly lower than our results (Wang, Hendy, Latimer, & Bilardello, 2019). Wang et al. (2019) observed Fe speciation similar to ours in some deeper samples, and they argue that elevated

sedimentation rates may have muted some of the Fe speciation ratios. Regardless, these sediment Fe speciation results are generally consistent with observations that the water column is reducing but not fully euxinic.

As outlined in Introduction, Tl isotopes from anoxic but non-euxinic sediments have not been previously investigated and the Tl isotope composition of such sediments and the overlying water column is unknown. There are no known marine localities that are direct analogs for the ferruginous conditions inferred for the ancient record given the large difference in oceanic sulfate concentrations. However, given these constraints, we posit that our understanding of the modern seawater redox state of the Santa Barbara Basin and the Fe speciation values from sediments reported here make it a reasonable, though not perfect, modern comparison to ancient anoxic but non-euxinic conditions.

Until now, the phases bearing Tl in non-euxinic reducing sediments have not been well understood. In euxinic basins, Tl is removed quantitatively through scavenging or incorporation into Fe sulfides precipitated from the water column below the chemocline

TABLE 1 (Continued)

Mo_{EF}	U_{EF}	Fe_{py} wt%	Fe_{carb} wt%	Fe_{oxide} wt%	Fe_{mag} wt%	Fe_{HR} wt%	Fe_{HR}/Fe_T	Fe_{py}/Fe_{HR}
374	5	0.09	0.06	1.07	–	1.22	0.53	0.07
87	6							
403	6	0.15	0.04	1.07	–	1.26	0.57	0.12
105	5							
11	8	0.04	0.13	1.64	–	1.80	0.54	0.02
3	2							
3	1	1.22	0.07	0.57	–	1.86	0.63	0.66
3	1							
50	10	0.01	–	1.37	–	1.38	0.51	0.01
100	8							
5	1	1.08	0.19	0.37	0.45	2.09	0.46	0.52
5	1	1.16	0.16	0.29	0.36	1.96	0.43	0.59
6	1	1.14	0.19	0.44	0.36	2.13	0.45	0.53
4	1	1.13	0.11	0.33	0.36	1.94	0.41	0.58

(Nielsen et al., 2011; Owens et al., 2017). Although non-euxinic reducing conditions can also support sulfide formation near the sediment–water interface, it is also possible that Tl incorporation in reducing sediments could occur through other processes. Studies of Tl sorption to organic-rich soils have concluded that Tl is not strongly bound to organic matter (Jacobson, McBride, Baveye, & Steenhuis, 2005), which indicates that Tl enrichment in ferruginous sediments is unlikely to originate from sorption to organic matter. We suggest that microbial sulfate reduction occurring at or near the sediment–water interface would provide free HS⁻ that combines with dissolved iron to precipitate pyrite and might be the likely mechanism for Tl deposition in ferruginous conditions. However, Tl concentrations in these sediments do not show any correlations with the Fe-pyrite content, suggesting that other mineral phases may have the capacity to accumulate Tl. In addition, assuming that all sulfate at the sediment–water interface was converted to HS⁻, the porewaters would still be more than three orders of magnitude undersaturated with respect to Tl_2S (Nielsen et al., 2011). Therefore, it is unlikely that Tl_2S would precipitate

directly from these waters. Alternatively, Tl could also be dominantly sorbed onto the surface of clay minerals in these non-euxinic reducing sediments, especially Na-illite (e.g., Martin, Wissocq, Benedetti, & Latrille, 2018; Voegelin et al., 2015). Given that Tl isotope fractionation appears to be muted during sorption that is not associated with Tl oxidation (Nielsen et al., 2013), it would not be expected that clay minerals are fractionated relative to the water column. However, future studies investigating possible Tl isotope fractionation during clay mineral adsorption would be needed to verify this hypothesis.

Regardless of the Tl enrichment process, the average Tl isotope composition of the four modern sediment samples from the Santa Barbara Basin is $\varepsilon^{205}Tl = -5.6 \pm 0.1$, which is within analytical uncertainty of the modern seawater value of $\varepsilon^{205}Tl = -6.0 \pm 0.3$. This similarity suggests that sediments deposited under reducing conditions with no evidence for local manganese oxide deposition—note that total Mn concentrations are much lower in SBB than average oxic sediments—may faithfully capture the Tl isotope composition of overlying oxic seawater in open marine settings,

akin to euxinic sediments (Owens et al., 2017). Therefore, Tl isotopic analysis of authigenic phases in marine sediments deposited under reducing conditions can potentially record the marine seawater value, which supports the proxy utilization in similar ancient environments.

5.2 | Local redox conditions in the Nanhua Basin

Most samples from the Baiguoyuan section have Fe speciation evidence consistent with deposition in predominantly ferruginous conditions (Figure 3a). Three samples from this section yielded lower Fe_{HR}/Fe_T values (0.22–0.38) that may have resulted from deposition under oxic water column conditions, but multiple scenarios could allow for similar values even under anoxic deposition: (a) high sedimentation rates and dilution of Fe_{HR} (Raiswell & Canfield, 1998), (b) loss of Fe(II) through the reduction of Fe oxide and then transfer into deeper water column (Lyons & Severmann, 2006), (c) the shallow marine trapping of Fe_{HR} under oxic water column conditions (e.g., Poulton & Raiswell, 2002), or (d) early diagenetic transformation of unsulfidized Fe to poorly reactive Fe-rich clays (in the absence of sulfide) (Poulton & Raiswell, 2002). The latter two processes commonly can be distinguished by near terrestrial input values or enrichments in Fe_T/Al above terrestrial input values (Lyons & Severmann, 2006). In contrast, the former two processes could possibly be consistent with low Fe_T/Al ratios (0.18–0.27) due to the loss of Fe (II) through iron shuttling and/or dilution of Fe_{HR} by rapid deposition of lithogenic material with low Fe/Al ratios. For example, Scholz et al. (2014) have reported low Fe_{HR}/Fe_T and Fe_T/Al ratios in the modern Peru margin oxygen minimum zone resulting from the loss of Fe (II) through Fe shuttling. Therefore, given the context of other similar data, the Fe speciation data from these three samples still likely record reducing conditions or close proximity to a ferruginous water column (Li et al., 2015).

For the Jiulongwan section, elevated Fe_{py}/Fe_{HR} ratios (>0.75) of most of the samples suggest dominantly euxinic conditions, which is consistent with previous studies of Fe speciation (Li et al., 2010; Och et al., 2015). Our Fe speciation data from the Chenjiayuanzi and Wuhe sections suggest predominantly ferruginous conditions for those samples (Figure 3a). However, we have only analyzed a very limited sample set from Wuhe and a more extensive study found almost exclusively euxinic conditions for Members III and IV in the Wuhe section (Sahoo et al., 2016). This may suggest that our data points are less representative of the predominant local redox conditions during deposition of Members III and IV at Wuhe, especially when considering the high trace metal concentrations presented herein.

In addition to Fe speciation, Mo_{EF} and U_{EF} are commonly used to identify water column redox conditions (Algeo & Tribovillard, 2009). Molybdenum is well known to enrich in sediments underlying sulfidic water columns due to the reactions of molybdate with water column sulfide to form tetrathiomolybdate, which

is particle-reactive and is efficiently buried with organic matter (Algeo & Lyons, 2006; Dahl, Chappaz, Fitts, & Lyons, 2013; Scott & Lyons, 2012). In contrast, uranium enrichment initiates at Eh conditions close to where Fe(III) reduction initiates, allowing the contrasting behavior with Mo to identify non-sulfidic anoxia versus euxinic conditions (Tribovillard et al., 2006). Elevated Mo (>100 ppm) and U concentrations are taken as evidence for deposition under euxinic water column conditions with a large marine metal inventory, while elevated U and lower Mo (<100 ppm; but >25 ppm) concentrations are indicative of anoxic, non-euxinic water column settings (Tribovillard et al., 2006).

The relationship between our Mo_{EF} and U_{EF} is in general agreement with the Fe speciation data that are indicative of anoxic conditions for most samples from the Baiguoyuan section, and euxinic water column conditions at the Jiulongwan section (Figure 3b). In contrast, the relationship between Mo_{EF} and U_{EF} for most shale samples from the Chenjiayuanzi section and the top of the Wuhe section could have been deposited in a euxinic environment (Figure 3b), whereas Fe speciation from these sections primarily implies ferruginous conditions (Figure 3a). Mo and U concentrations in this study are very similar to those reported by Sahoo et al. (2016), which at least indicates no loss of Mo and U even though oxidative weathering has occurred at the outcrop. However, oxidative weathering may transfer pyrite to Fe oxide, which may be a possible explanation for the low contribution of Fe_{py} relative to the Fe_{HR} pool in these samples. Regardless, the Fe_{HR} concentrations would be minimally affected by such a process and would not impact our assessment that the sediments were deposited under anoxic conditions (Canfield et al., 2008). If we assume that all Fe oxide in the Chenjiayuanzi and Wuhe sections represent oxidized pyrite, then most samples would plot above the euxinic threshold. In this scenario, our trace element data would support the previous conclusions by Sahoo et al. (2016) that Members III and IV in these locations were primarily deposited under euxinic conditions.

In summary, we conclude that our new Fe speciation and trace element data for the four sections studied here are broadly indicative of deposition under anoxic water conditions. Detailed interpretations of these data indicate mostly ferruginous conditions locally during the Shuram NCIE with some samples deposited under euxinic conditions, predominantly in the Jiulongwan and Wuhe sections. Combined with previously published data on sediments from the Nanhua Basin (Och et al., 2015; Sahoo et al., 2016), we argue that these general local redox conditions are broadly applicable throughout this basin during the Shuram NCIE.

5.3 | Stratigraphic Tl isotope correlation of the four sections

A high-resolution section-by-section stratigraphic correlation is difficult in the Nanhua Basin due to the lack of event stratigraphic marker beds or diagnostic fossil occurrences. However, we can examine the general characteristics of the Tl isotope compositions
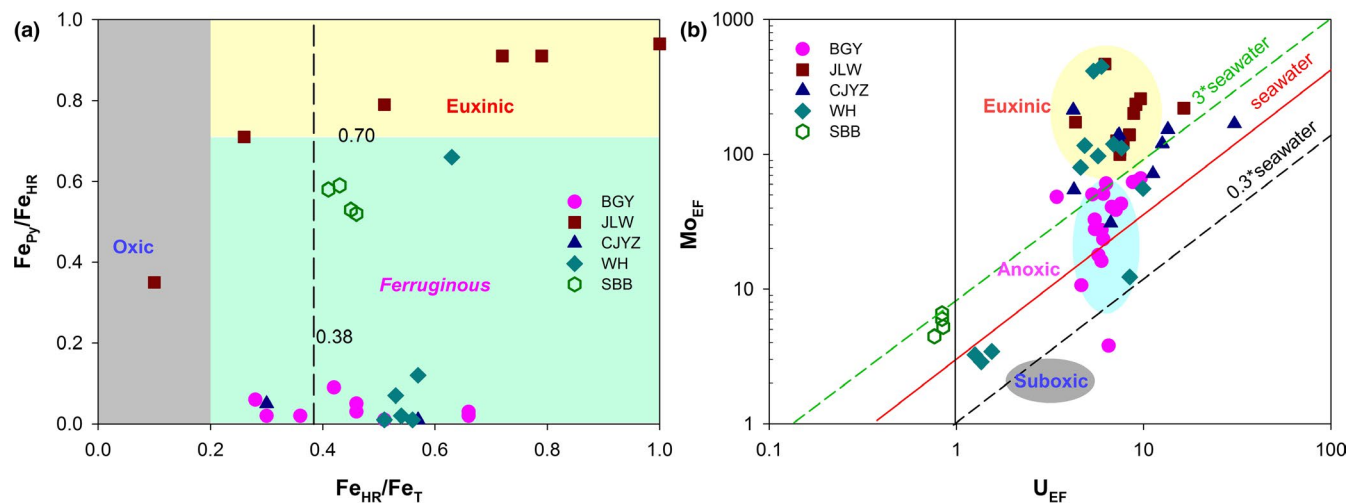
FIGURE 3 The local redox conditions of four investigated sections and the Santa Barbara Basin are reflected by Fe species data (a) and MoEF-UEF covariation (b). The red line shows Mo/U molar ratios equal to the seawater value (7.5–7.9), and black and green dash lines, equal to fractions thereof (0.3*SW, 3*SW), respectively (Algeo & Tribovillard, 2009) (b). BGY, Baiguoyuan; CJYZ, Chenjiayuanzi; JLW, Jiulongwan; SBB, the Santa Barbara Basin; WH, Wuhe
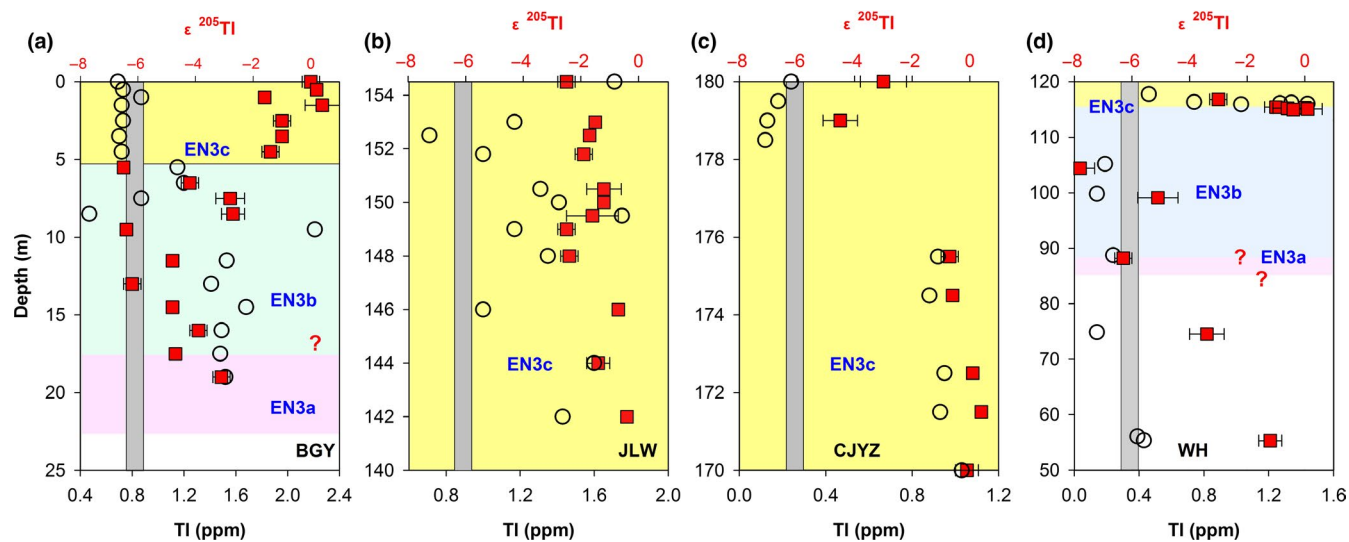

FIGURE 4 Tl concentrations and isotope compositions during the Shuram NCIE along four investigated sections. Gray columns represent the modern oxic seawater value of $\varepsilon^{205}Tl = -6$

in each of the three stratigraphically subdivided intervals of the Shuram NCIE (EN3a-b-c) that have previously been documented (Figure 2). There is a general agreement of Tl isotope values in intervals EN3b and EN3c that are recorded at the Baiguoyuan and Wuhe sections (Figure 4), which suggests that the Tl isotope composition of the Nanhua Basin was relatively homogenous throughout the Shuram NCIE during these periods. Period EN3a is only represented by samples from the Baiguoyuan section, and we can therefore not assess whether the Nanhua Basin was homogeneous with respect to Tl isotopes during this period. However, in general the Tl isotope similarity between the four sections supports that the Tl isotope composition of the Nanhua Basin was relatively homogeneous during the Shuram NCIE and that the sections largely record the Tl isotopic evolution of the water mass within the basin. A schematic

depiction in Figure 5 shows the Tl isotopic evolution of the Nanhua Basin during the Shuram NCIE. However, based on our current knowledge of the basin it is difficult to confidently assess whether this Tl isotope evolution reflects the global ocean or could be due to changes in basinal restriction. It has been shown that basinal restriction in the Black Sea causes the Tl isotope composition of this basin to closely reflect the riverine input values of $\varepsilon^{205}Tl \approx -2$ (Owens et al., 2017), whereas the Cariaco Basin (Owens et al., 2017) and Santa Barbara Basin (this study) are sufficiently well connected to the open ocean that the sediments record open ocean oxic seawater values. The Nanhua Basin, and the Jiulongwan and Wuhe sections, in particular, has been inferred to be well connected to the open ocean (Jiang et al., 2003; Och et al., 2015; Sahoo et al., 2016; Zhang et al., 2013; Zhu et al., 2013), which would suggest that the depositional

environment in the Nanhua Basin was more similar to that found in the Santa Barbara and Cariaco Basins rather than the Black Sea. If this is indeed the case, then the Tl isotope evolution of the Nanhua Basin during the Shuram NCIE would reflect that of the global ocean. In the absence of any sedimentological and geochemical evidence for basinal restriction in the Nanhua Basin, we here interpret the Tl isotope curve as an open ocean record, but caution that basinal restriction in the Nanhua Basin would likely have caused Tl isotopic compositions of the water column to converge toward the crustal input value of ε^{205}Tl ≈ −2, assuming the local inputs had the same composition as modern rivers.

5.3.1 | Effect of oxidative weathering on Tl isotopes

The same Tl isotope composition between upper continental crust (ε^{205}Tl = −2.0) and riverine detrital particulates (ε^{205}Tl = −2.5) has indicated negligible Tl isotope fractionation during continental weathering processes (Nielsen et al., 2005). However, Tl isotope fractionation by direct weathering remains relatively unexplored. A recent study of lateritic soil profiles suggested that Tl is leached out from the soil during continental oxidative weathering, which is associated with small and resolvable Tl isotope fractionation toward heavy values (from −2.2 to +0.3) in the residual soil (Howarth, Prytulak, Little, Hammond, & Widdowson, 2018). These authors also observed Tl enrichment and heavy ε^{205}Tl values (+6) at the paleowater table in another basalt-base profile, which likely reflected an external source of Tl and significant isotope fractionation controlled by Fe-Mn oxides (Howarth et al., 2018). Neither of these processes are capable of explaining the very light Tl isotope signatures observed for shales from the EN3a and EN3b intervals, which eliminates weathering as a possible cause for most of our Tl isotope variation. External addition of Tl, either as a syndepositional Fe-Mn shuttle or as a post-depositional Fe-Mn oxide precipitation, could account for some of the heaviest values (ε^{205}Tl ~ 0). However, given that these heavy values are observed at similar stratigraphic levels in all four sections, the latter of these options appear less likely.

5.3.2 | Near-modern oxic seawater Tl isotopes

We interpret the Tl isotope value of ε^{205}Tl ≈ −8 to −5 during the Shuram NCIE as evidence for near-modern Mn oxide burial fluxes. Thallium isotopes show a gradually decreasing trend from ε^{205}Tl ~ −3 to −5 during EN3a-EN3b transition, and then generally record values of ε^{205}Tl ~ −8 to −5 during EN3b interval (Figures 4a,d and 5). This negative Tl isotope excursion may reflect increased global Tl scavenging by Mn oxide burial. The increase in Mn oxide burial during the EN3a to EN3b can be modeled using a previously published isotope mass balance model, $\varepsilon_{sw} = \varepsilon_{IN} * F_{IN} - \Delta_{MnOX} * (F_{MnOX}/F_{IN}) - \Delta_{AOC} * (F_{AOC}/F_{IN})$ (Nielsen et al., 2009; Ostrander et al., 2017). In this model, ε_{sw} and ε_{IN} are the Tl isotope compositions of seawater and total inputs, where ε_{IN} is effectively constant (ε^{205}Tl = −2,

Baker et al., 2009; Nielsen et al., 2011, 2005, 2017, 2006). Δ_{MnOX} and Δ_{AOC} are the Tl isotope fractionation between seawater and Mn oxide and altered oceanic crust (AOC). F_{IN}, F_{MnOX}, and F_{AOC} are the total inputs, Mn oxide, and AOC output fluxes, respectively. The shift from ε^{205}Tl ~ −3 to near or slightly lower than modern seawater values during the EN3a to EN3b transition can be explained by Mn oxide output fluxes that increased by approximately 30%, assuming $\Delta_{MnOX-seawater}$ = +16 ε^{205}Tl-units and $\Delta_{AOC-seawater}$ = −1.1 ε^{205}Tl-units. Previous studies suggested that significant Mn oxide burial required high concentration of molecular oxygen or O_2-derived species, such as superoxide, available in the water column (Johnson et al., 2016). As noted earlier, the Tl isotope composition of authigenic Tl in our black shales during the Shuram NCIE most likely reflects that of open ocean seawater. Therefore, this large-scale increase in Mn oxide burial likely reflects an increased capacity of the ocean to oxidize Mn, either through increased O_2-derived species, such as superoxide, in the oxygenic portion of the water column, or via an expansion of areas capable of burying Mn oxide, possibly due to increased oxygen at the sediment–water interface in the global ocean (Ostrander et al., 2019). Although the Mn oxide burial rates required to produce ε^{205}Tl ~ −6 are high, it remains difficult to quantify ocean oxygenation due to uncertainties associated with the link between the global modern Mn budget and quantifying the overall ocean oxygen budget. Due to the likely ferruginous conditions in the deep ocean (e.g., Canfield et al., 2008), the marine Mn reservoir should have been much larger than it is today, which would have enhanced the capacity of the ocean to precipitate large amounts of Mn oxide over extended periods of time. Thus, any increase in ocean oxygenation would likely have triggered large changes in Mn oxide precipitation.

Despite the inability to use Tl isotopes to directly constrain ocean oxygenation, our interpretation of increased ocean oxygenation at the EN3a to EN3b transition is consistent with previously reported evidence for an oxygenation event during this time, which was based on globally enhanced continental weathering (Li et al., 2017; Sawaki et al., 2010), elevated marine sulfate concentrations and decreased sulfur isotope composition (Fike et al., 2006; Kaufman et al., 2007; Li et al., 2017; Loyd et al., 2013; Osburn et al., 2015), elevated marine iodate concentrations observed in a range of global depositional settings (Hardisty et al., 2017), and a positive U isotope excursion (Kendall et al., 2015; Zhang et al., 2019). Although spatially heterogeneous, paired δ^{13}C and δ^{34}S records show coincident negative excursions interpreted to represent an event that oxidized large dissolved organic carbon and sulfide pools in the deep oceans (Fike et al., 2006; Kaufman et al., 2007; Li et al., 2017; Loyd et al., 2013; Osburn et al., 2015; Shi et al., 2018). Coincident with the Shuram NCIE records, I/(Ca + Mg) ratios from three separate paleocontinents have been shown to shift to higher values indicating the presence of locally oxic water columns in these shallow carbonate environments (Hardisty et al., 2017). Our new Tl isotope measurements show near-modern seawater values during most of the EN3b interval. Coupling our data with previously published independent geochemical proxy data sets, hence, provides additional

evidence for an oxidation event in the global oceans during the EN3a-to-EN3b transition, which based on Tl isotopes may suggest that the Mn oxide burial flux was similar to or greater than that of the modern ocean. Given the coupled relationship between Tl and C isotope curves during the Shuram NCIE in our investigated sections (Figure 5), we argue that the oxygenation of a large water mass in the global oceans during the Ediacaran may have been a pivotal trigger for the Shuram NCIE through the oxidation of a large dissolved organic carbon reservoir, the disappearance of acanthomorph acritarchs, and the radiation of Ediacaran-type biota (e.g., Fike et al., 2006; McFadden et al., 2008).

5.3.3 | Tl isotopes during recovery from the Shuram NCIE

Thallium isotopes document a sharp increase at the EN3b-EN3c transition (Figures 4 and 5), and during the late period of the Shuram NCIE (EN3c), nearly all samples from our four sections deposited under euxinic and ferruginous conditions show Tl isotope values near or slightly higher than modern inputs. Similar increases in Tl isotopes have been observed in two Mesozoic Oceanic Anoxic

Events and a Paleozoic event, and these were suggested to be due to a decrease in Mn oxide burial in the global oceans (Bowman et al., 2019; Ostrander et al., 2017; Them et al., 2018). This mechanism may be a potential trigger for the observed increase in Tl isotope values around the EN3b-EN3c boundary. It is important to note that Tl burial into AOC likely has varied over Earth history, but that over geologically shorter (<5 Myrs) events, the AOC flux is probably relatively invariant (Nielsen et al., 2009). Therefore, it is reasonable to compare these Phanerozoic events with the Shuram NCIE in terms of the similarly observed rapid Tl isotope changes.

However, in contrast to Phanerozoic deoxygenation events where dissolved oceanic Mn was likely already very low, the decrease in Mn oxide burial during the Shuram NCIE could either be due to a diminished dissolved Mn reservoir in the ocean or a contraction of the seafloor area with oxygen at the sediment–water interface. The first scenario would not require a change in the oxygenation of the ocean, merely implying that so much reduced dissolved Mn had been removed from the ocean that Mn oxide burial fluxes eventually began to decrease. As such, the positive Tl isotope shift toward the end of the Shuram NCIE does not require a global ocean deoxygenation event. It is notable that the Tl isotope shift toward heavier values occurs before the recovery back to heavier C isotope compositions
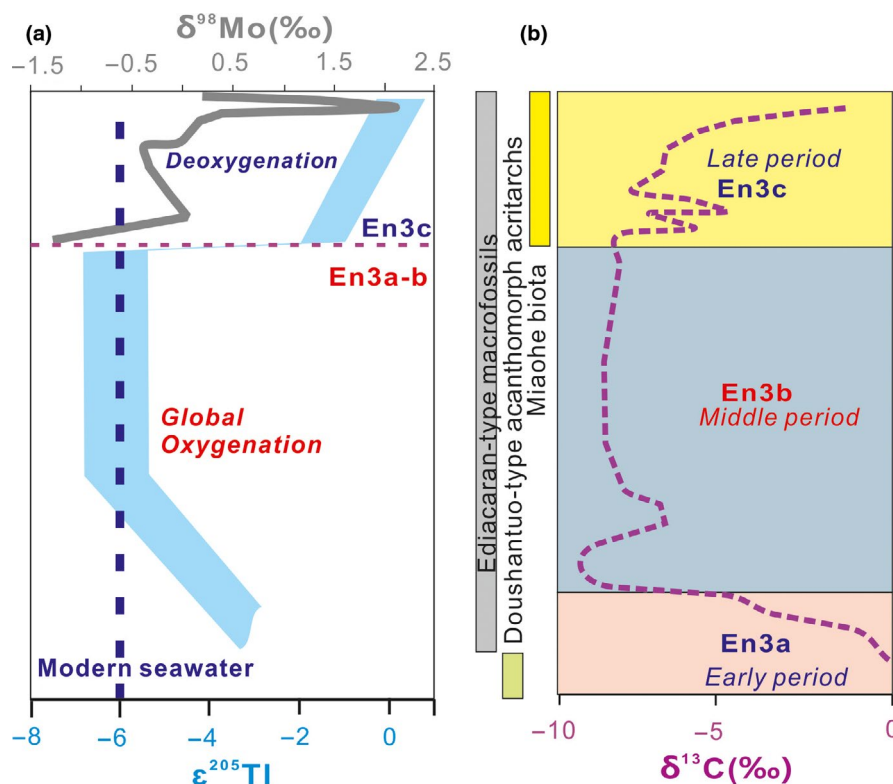

FIGURE 5 A schematic depiction of the Tl isotopic evolution of the Nanhua Basin during the Shuram NCIE, correlated with Mo and carbon isotopes. (a) Tl isotope conceptual curve in this study and Mo isotope curve reported by Kendall et al. (2015) during the Shuram NCIE. (b) The carbon isotope curve of the Yangtze Gorges area (Li et al., 2010, 2017; McFadden et al., 2008) can be divided into the early (EN3a), middle (EN3b), and late (EN3c) excursion intervals. The possible appearance of complex macroscopic metazoans is also marked along the Shuram NCIE. Doushantuo-type acanthomorph acritarchs seem to be restricted to before the Shuram NCIE in South China, South Australia, and Siberia (Xiao et al., 2016, and reference therein). Ediacaran-type macrofossils consist macroscopic, soft-bodied, morphologically complex, and phylogenetically diverse eukaryotes including animals, which is geographically worldwide and found in 575-541 Ma rocks of the late Ediacaran period (Xiao et al., 2016)

(Figure 5). If the Shuram NCIE is related to DOC oxidation (Fike et al., 2006; Jiang et al., 2007; McFadden et al., 2008; Rothman et al., 2003), then the earlier shift in Tl isotopes could be consistent with either exhaustion of the dissolved reduced Mn reservoir from the deep ocean before total DOC oxidation, or a decrease in the area of the seafloor in contact with oxygenated seawater at the sediment–water interface before organic carbon burial re-commenced and caused the end of the Shuram NCIE. The latter mechanism would be similar to the interpretation for the Phanerozoic events where the Tl isotope composition of seawater was observed to respond prior to the carbon isotope excursion (Ostrander et al., 2017; Them et al., 2018; Bowman et al., 2019; and reviewed in Owens, 2019). The decreasing U isotope (δ^{235}U) composition of seawater recorded by shales from the Member IV of the Doushantuo Formation and carbonate from the Nama Group suggested a rapid and dramatic anoxic expansion from ~560–550 Ma (Kendall et al., 2015; Tostevin et al., 2019; Zhang et al., 2019), providing additional evidence for our proposed decrease in ocean oxygenation during the EN3c.

In addition, low δ^{98}Mo values (<0.7‰) have been found in most shales from the lower part of Member IV in the Jiulongwan section (e.g., EN3c), which was interpreted to reflect Mo isotope fractionation in weakly sulfidic waters or by the accumulation in the sediments of Mo that was previously adsorbed onto Mn oxide particles (Figure 5; Kendall et al., 2015). If the latter process was in operation, then we would expect significantly heavier Tl isotope compositions than the contemporaneous seawater value ε^{205}Tl ≤-2, because Mn oxides are ~16 ε^{205}Tl-units heavier than the water from which they precipitate (Nielsen et al., 2013; Rehkämper et al., 2002). Some Tl isotope compositions in the EN3c interval at all four sections approach ε^{205}Tl = 0 (Figure 4), which could be consistent with Fe-Mn oxide shuttling, but not with effects from weathering (see Section 5.3.1 for details). However, all four sections we investigated represent significantly different positions within the Nanhua Basin. In general, Fe-Mn oxide shuttling might be expected to operate most strongly in proximity to a chemocline within a basin as the oxide minerals (in particular, Mn oxides) most likely require dissolved oxygen for precipitation and then rapidly re-dissolve once they reach an anoxic water masses (Rue et al., 1997). Hence, the ubiquity of the near crustal ε^{205}Tl values throughout the Nanhua Basin suggests this to be a feature of the entire basin, rather than a product of Fe-Mn shuttling processes. Moreover, high δ^{235}U values in Member IV from the Jiulongwan section also do not support the operation of Fe-Mn shuttling in the local deposition environment, because Fe-Mn oxide sinks commonly enrich isotopically light U (Kendall et al., 2015 and references therein). Future work is needed on the exact effects of Fe-Mn oxide shuttling on sediment isotopic signature of Mo and Tl, as well, as trace metal concentrations to improve constraints on how to interpret the trace element and stable isotopic signatures observed in the EN3c interval.

High δ^{98}Mo values (1.7–2.0‰) at the latest stage of EN3c in one small interval from the Jiulongwan section (Figure 5; Kendall et al., 2015) are difficult to correlate directly with our Tl isotope data, and even though our samples were collected from the same formation,

sample coverage may not be consistent between these two studies. We therefore cannot use our present data set to evaluate whether the short oxygenation period proposed by Kendall et al. (2015) is supported by the occurrence of light Tl isotope compositions. In addition, the Tl could be responding faster to deoxygenation (or reduction in oceanic Mn reservoir) than Mo and U, due to the difference in modern residence times for these three elements. Nevertheless, if our proposed deoxygenation event during the uppermost portion of the Shuram NCIE indeed occurred, we can argue that the oxygenation event during the EN3a-b intervals could have stimulated the evolution of Ediacaran-type biota (e.g., McFadden et al., 2008; Zhang et al., 2019) and the subsequent deoxygenation event during EN3c did not prevent the appearance of macroscopic mobile bilaterians (Figure 5).

6 | CONCLUSION

In this contribution, we show that the Tl isotope composition of the authigenic component in sediments from the reducing Santa Barbara Basin is identical to the open ocean seawater value. These data imply that Tl isotope compositions of reducing, non-euxinic ancient sediments can be used to reconstruct the Tl isotope composition of contemporaneous seawater. This finding indicates that anoxic, non-euxinic—as well as euxinic—sediments from basins well connected to the open ocean can be utilized for Tl isotope redox proxy reconstructions (Owens et al., 2017).

We also have applied the Tl isotope proxy in ancient ferruginous and euxinic shales deposited during the late Ediacaran that record the Shuram NCIE in the Doushantuo Formation from four sections (that span the inner shelf to the continental slope) in South China. During the peak of the Shuram NCIE, values of the ferruginous/euxinic shales from both the inner shelf (Baiguoyuan) and slope (Wuhe) sections show light Tl isotope values (ε^{205}Tl = −5 to −8), with an average value close to the modern oxic seawater value of ε^{205}Tl = −6. These values are lighter than values observed at the onset and recovery stages of the Shuram NCIE. These lighter values suggest a significant increase in Mn oxide burial fluxes during the main phase of the Shuram NCIE. This increase in Mn oxide burial could correspond to an expansion of the seafloor area with high oxygen concentrations at the sediment–water interface. Alternatively, the increased Mn oxide burial could also have been induced by an increased oxidative capacity of the oxic portion of an otherwise anoxic ocean that would have steadily depleted the anoxic portion of the ocean in dissolved Mn. In either case, the contemporaneous negative Tl and C isotope excursions during the early–middle stage of Shuram NCIE suggest that the origin of the Shuram NCIE and the radiation of Ediacaran-type biota are likely associated with a large-scale or possibly even global ocean oxygenation event.

CONFLICT OF INTEREST

The authors declare no conflict of interest and no competing financial interests.

AUTHOR CONTRIBUTIONS

H.F. and S.N. conceived the study and performed research. H.F. and H.W. collected samples and analyzed major and trace elements. H.F., M.A., Y.S., and J.O. analyzed Tl isotope data. C.B., J.O., and S.Y. analyzed Fe species data. H.F. wrote the manuscript with contributions from S.N., J.O., D.H., S.Y., C.B., T.H., and H.W. All authors contributed to discussions.

ORCID

Haifeng Fan https://orcid.org/0000-0003-0080-2700

REFERENCES

Algeo, T. J., & Lyons, T. W. (2006). Mo-total organic carbon covariation in modern anoxic marine environments: Implications for analysis of paleoredox and paleohydrographic conditions. *Paleoceanography, 21*(1), PA1016. https://doi.org/10.1029/2004PA001112

Algeo, T. J., & Tribovillard, N. (2009). Environmental analysis of paleoceanographic systems based on molybdenum–uranium covariation. *Chemical Geology, 268*, 211–225. https://doi.org/10.1016/j.chemgeo.2009.09.001

Baker, R. G. A., Rehkämper, M., Hinkley, T. K., Nielsen, S. G., & Toutain, J. P. (2009). Investigation of thallium fluxes from subaerial volcanism—Implications for the present and past mass balance of thallium in the oceans. *Geochimica et Cosmochimica Acta, 73*, 6340–6359. https://doi.org/10.1016/j.gca.2009.07.014

Berner, R. A. (1982). Burial of organic carbon and pyrite sulfur in the modern ocean: Its geochemical and environmental significance. *American Journal of Science, 282*(4), 451–473. https://doi.org/10.2475/ajs.282.4.451

Bowman, C. N., Young, S. A., Kaljo, D., Eriksson, M. E., Them, T. R., Hints, O., ... Owens, J. D. (2019). Linking the progressive expansion of reducing conditions to a stepwise mass extinction event in the late Silurian oceans. *Geology, 47*(10), 968–972. https://doi.org/10.1130/G46571.1

Bristow, T. F., & Kennedy, M. J. (2008). Carbon isotope excursions and the oxidant budget of the Ediacaran atmosphere and ocean. *Geology, 36*, 863–866. https://doi.org/10.1130/G24968A.1

Calver, C. R. (2000). Isotope stratigraphy of the Ediacarian (Neoproterozoic III) of the Adelaide Rift Complex, Australia, and the overprint of water column stratification. *Precambrian Research, 100*, 121–150. https://doi.org/10.1016/S0301-9268(99)00072-8

Canfield, D. E., Poulton, S. W., Knoll, A. H., Narbonne, G. M., Ross, G., Godlberg, T., & Strauss, H. (2008). Ferruginous conditions dominated later-Neoproterozoic deep-water chemistry. *Science, 321*, 949–952. https://doi.org/10.1126/science.1154499

Canfield, D. E., Raiswell, R., Westrich, J. T., Reaves, C. M., & Berner, R. A. (1986). The use of chromium reduction in the analysis of reduced inorganic sulfur in sediments and shales. *Chemical Geology, 54*(1–2), 149–155. https://doi.org/10.1016/0009-2541(86)90078-1

Condon, D., Zhu, M. Y., Bowring, S., Wang, W., Yang, A. H., & Jin, Y. G. (2005). U-Pb ages from the Neoproterozoic Doushantuo Formation, China. *Science, 308*(5718), 95–98.

Dahl, T. W., Chappaz, A., Fitts, J. P., & Lyons, T. W. (2013). Molybdenum reduction in a sulfidic lake: Evidence from X-ray absorption fine-structure spectroscopy and implications for the Mo paleoproxy. *Geochimica et Cosmochimica Acta, 103*, 213–231. https://doi.org/10.1016/j.gca.2012.10.058

Fike, D. A., Grotzinger, J. P., Pratt, L. M., & Summons, R. E. (2006). Oxidation of the Ediacaran ocean. *Nature, 444*(7120), 744–747.

Grotzinger, J. P., Fike, D. A., & Fischer, W. W. (2011). Enigmatic origin of the largest-known carbon isotope excursion in Earth's history. *Nature Geoscience, 4*, 285–292. https://doi.org/10.1038/ngeo1138

Han, T., & Fan, H. F. (2015). Dynamic evolution of the Ediacaran ocean across the Doushantuo Formation, South China. *Chemical Geology, 417*, 261–272. https://doi.org/10.1016/j.chemgeo.2015.09.021

Hardisty, D. S., Lu, Z., Bekker, A., Diamond, C. W., Gill, B. C., Jiang, G., ... Lyons, T. W. (2017). Perspectives on Proterozoic surface ocean redox from iodine contents in ancient and recent carbonate. *Earth and Planetary Science Letters, 463*, 159–170. https://doi.org/10.1016/j.epsl.2017.01.032

Howarth, S., Prytulak, J., Little, S. H., Hammond, S. J., & Widdowson, M. (2018). Thallium concentration and thallium isotope composition of lateritic terrains. *Geochimica et Cosmochimica Acta, 239*, 446–462. https://doi.org/10.1016/j.gca.2018.04.017

Jacobson, A. R., McBride, M. B., Baveye, P., & Steenhuis, T. S. (2005). Environmental factors determining the trace-level sorption of silver and thallium to soils. *Science of the Total Environment, 345*, 191–205. https://doi.org/10.1016/j.scitotenv.2004.10.027

Jiang, G. Q., Kaufman, A. J., Christie-Blick, N., Zhang, S. H., & Wu, H. C. (2007). Carbon isotope variability across the Ediacaran Yangtze platform in South China: Implications for a large surface-to-deep ocean δ^{13}C gradient. *Earth and Planetary Science Letters, 261*, 303–320. https://doi.org/10.1016/j.epsl.2007.07.009

Jiang, G. Q., Shi, X. Y., Zhang, S. H., Wang, Y., & Xiao, S. H. (2011). Stratigraphy and paleogeography of the Ediacaran Doushantuo Formation (ca. 635–551Ma) in South China. *Gondwana Research, 19*, 831–849. https://doi.org/10.1016/j.gr.2011.01.006

Jiang, G. Q., Sohl, L. E., & Christie-Blick, N. (2003). Neoproterozoic stratigraphic comparison of the Lesser Himalaya (India) and Yangtze block (south China): Paleogeographic implications. *Geology, 31*(10), 917–920. https://doi.org/10.1130/G19790.1

Johnson, J. E., Webb, S. M., Ma, C., & Fischer, W. W. (2016). Manganese mineralogy and diagenesis in the sedimentary rock record. *Geochimica et Cosmochimica Acta, 173*, 210–231. https://doi.org/10.1016/j.gca.2015.10.027

Kaufman, A. J., Corsetti, F. A., & Varni, M. A. (2007). The effect of rising atmospheric oxygen on carbon and sulfur isotope anomalies in the Neoproterozoic Johnnie Formation, Death Valley, USA. *Chemical Geology, 237*, 47–63. https://doi.org/10.1016/j.chemgeo.2006.06.023

Kendall, B., Komiya, T., Lyons, T. W., Bates, S. M., Gordon, G. W., Romaniello, S. J., ... Anbar, A. D. (2015). Uranium and molybdenum isotope evidence for an episode of widespread ocean oxygenation during the late Ediacaran Period. *Geochimica et Cosmochimica Acta, 156*, 173–193. https://doi.org/10.1016/j.gca.2015.02.025

Le Guerroué, E., Allen, P. A., Cozzi, A., Etienne, J. L., & Fanning, M. (2006). 50Myr recovery from the largest negative δ^{13}C excursion in the Ediacaran ocean. *Terra Nova, 18*, 147–153.

Li, C., Hardisty, D. S., Luo, G., Huang, J., Algeo, T. J., Cheng, M., ... Lyons, T. W. (2017). Uncovering the spatial heterogeneity of Ediacaran

carbon cycling. *Geobiology*, 15(2), 211–224. https://doi.org/10.1111/gbi.12222

Li, C., Love, G. D., Lyons, T. W., Fike, D. A., Sessions, A. L., & Chu, X. (2010). A stratified redox model for the Ediacaran Ocean. *Science*, 328(5974), 80–83.

Li, C., Planavsky, N. J., Shi, W., Zhang, Z., Zhou, C., Cheng, M., … Xie, S. (2015). Ediacaran marine redox heterogeneity and early animal ecosystems. *Scientific Reports*, 5, 17097. https://doi.org/10.1038/srep17097

Li, F. H., Yang, G. Z., Yao, Y., Liao, Z. M., Liu, S. D., He, H. T., & Tian, D. C. (2014). Basic characteristics and metallogenic model of Baiguoyuan silver-vanadium deposition in Xingshan county, Hubei Province. *Resources Environment and Engineering*, 28(3), 247–256. (In Chinese with English abstract)

Liu, P. J., Chen, S. M., Zhu, M. Y., Li, M., Yin, C. Y., & Shang, X. D. (2014). High-resolution biostratigraphic and chemostratigraphic data from the Chenjiayuanzi section of the Doushantuo Formation in the Yangtze Gorges area, South China: Implication for subdivision and global correlation of the Ediacaran System. *Precambrian Research*, 249, 199–214. https://doi.org/10.1016/j.precamres.2014.05.014

Loyd, S. J., Marenco, P. J., Hagadorn, J. W., Lyons, T. W., Kaufman, A. J., Sour-Tovar, F., & Corsetti, F. A. (2013). Local δ^{34}S variability in ~580 Ma carbonates of northwestern Mexico and the Neoproterozoic marine sulfate reservoir. *Precambrian Research*, 224, 551–569. https://doi.org/10.1016/j.precamres.2012.10.007

Lyons, T. W., & Severmann, S. (2006). A critical look at iron paleoredox proxies: New insights from modern euxinic marine basins. *Geochimica et Cosmochimica Acta*, 70, 5698–5722. https://doi.org/10.1016/j.gca.2006.08.021

Martin, L. A., Wissocq, A., Benedetti, M. F., & Latrille, C. (2018). Thallium (Tl) sorption onto illite and smectite: Implications for Tl mobility in the environment. *Geochimica et Cosmochimica Acta*, 230, 1–16. https://doi.org/10.1016/j.gca.2018.03.016

März, C., Poulton, S. W., Beckmann, B., Küster, K., Wagner, T., & Kasten, S. (2008). Redox sensitivity of P cycling during marine black shale formation: Dynamics of sulfidic and anoxic, non-sulfidic bottom waters. *Geochimica et Cosmochimica Acta*, 72, 3703–3717. https://doi.org/10.1016/j.gca.2008.04.025

McFadden, K. A., Huang, J., Chu, X., Jiang, G., Kaufman, A. J., Zhou, C., … Xiao, S. (2008). Pulsed oxidation and biological evolution in the Ediacaran Doushantuo Formation. *Proceedings of the National Academy of Sciences of the United States of America*, 105, 3197–3202. https://doi.org/10.1073/pnas.0708336105

Minguez, D., Kodama, K. P., & Hillhouse, J. W. (2015). Paleomagnetic and cyclostratigraphic constraints on the synchroneity and duration of the shuram carbon isotope excursion, johnnie formation, death valley region, CA. *Precambrian Research*, 266, 395–408. https://doi.org/10.1016/j.precamres.2015.05.033

Moffitt, S. E., Hill, T. M., Ohkushi, K., Kennett, J. P., & Behl, R. J. (2014). Vertical oxygen minimum zone oscillations since 20ka in Santa Barbara Basin: A benthic foraminiferal community perspective. *Paleoceanography*, 29, 44–57.

Narbonne, G. M. (2005). THE EDIACARA BIOTA: Neoproterozoic origin of animals and their ecosystems. *Annual Review of Earth and Planetary Sciences*, 33, 421–442. https://doi.org/10.1146/annurev.earth.33.092203.122519

Nielsen, S. G., Goff, M., Hesselbo, S. P., Jenkyns, H. C., LaRowe, D. E., & Lee, C.-T.-A. (2011). Thallium isotopes in early diagenetic pyrite – A paleoredox proxy? *Geochimica et Cosmochimica Acta*, 75, 6690–6704. https://doi.org/10.1016/j.gca.2011.07.047

Nielsen, S. G., Mar-Gerrison, S., Gannoun, A., LaRowe, D., Klemm, V., Halliday, A. N., … Hein, J. R. (2009). Thallium isotope evidence for a permanent increase in marine organic carbon export in the early Eocene. *Earth and Planetary Science Letters*, 278, 297–307. https://doi.org/10.1016/j.epsl.2008.12.010

Nielsen, S. G., Rehkämper, M., Baker, J., & Halliday, A. N. (2004). The precise and accurate determination of thallium isotope compositions and concentrations for water samples by MC-ICPMS. *Chemical Geology*, 204, 109–124. https://doi.org/10.1016/j.chemgeo.2003.11.006

Nielsen, S. G., Rehkämper, M., Porcelli, D., Andersson, P., Halliday, A. N., Swarzenski, P. W., … Günther, D. (2005). Thallium isotope composition of the upper continental crust and rivers—An investigation of the continental sources of dissolved marine thallium. *Geochimica et Cosmochimica Acta*, 69, 2007–2019. https://doi.org/10.1016/j.gca.2004.10.025

Nielsen, S. G., Rehkämper, M., & Prytulak, J. (2017). Investigation and application of thallium isotope fractionation. *Reviews in Mineralogy and Geochemistry*, 82, 759–798. https://doi.org/10.2138/rmg.2017.82.18

Nielsen, S. G., Rehkämper, M., Teagle, D. A. H., Butterfield, D. A., Alt, J. C., & Halliday, A. N. (2006). Hydrothermal fluid fluxes calculated from the isotopic mass balance of thallium in the ocean crust. *Earth and Planetary Science Letters*, 251, 120–133. https://doi.org/10.1016/j.epsl.2006.09.002

Nielsen, S. G., Wasylenki, L. E., Rehkämper, M., Peacock, C. L., Xue, Z. C., & Moon, E. M. (2013). Towards an understanding of thallium isotope fractionation during adsorption to manganese oxides. *Geochimica et Cosmochimica Acta*, 117, 252–265. https://doi.org/10.1016/j.gca.2013.05.004

Och, L. M., Cremonese, L., Shields-Zhou, G. A., Poulton, S. W., Struck, U., Ling, H. F., … Strauss, H. (2015). Palaeoceanographic controls on spatial redox distribution over the Yangtze Platform during the Ediacaran-Cambrian transition. *Sedimentology*, 63(2), 378–410.

Osburn, M. R., Owens, J., Bergmann, K. D., Lyons, T. W., & Grotzinger, J. P. (2015). Dynamic changes in sulfate sulfur isotopes preceding the Ediacaran Shuram Excursion. *Geochimica et Cosmochimica Acta*, 170, 204–224. https://doi.org/10.1016/j.gca.2015.07.039

Ostrander, C. M., Nielsen, S. G., Owens, J. D., Kendall, B., Gordon, G. W., Romaniello, S. J., & Anbar, A. D. (2019). Fully oxygenated water columns over continental shelves before the Great Oxidation Event. *Nature Geoscience*, 12, 186–191. https://doi.org/10.1038/s41561-019-0309-7

Ostrander, C. M., Owens, J. D., & Nielsen, S. G. (2017). Constraining the rate of oceanic deoxygenation leading up to a Cretaceous Oceanic Anoxic Event (OAE-2: ~94 Ma). *Science Advances*, 3(8), e1701020. https://doi.org/10.1126/sciadv.1701020

Owens, J. D. (2019). *Applications of thallium isotopes (elements in geochemical tracers in earth system science)*. Cambridge, UK: Cambridge University Press.

Owens, J. D., Nielsen, S. G., Horner, T. J., Ostrander, C. M., & Peterson, L. C. (2017). Thallium-isotopic compositions of euxinic sediments as a proxy for global manganese-oxide burial. *Geochimica et Cosmochimica Acta*, 213, 291–307. https://doi.org/10.1016/j.gca.2017.06.041

Poulton, S. W., & Canfield, D. E. (2005). Development of a sequential extraction procedure for iron: Implications for iron partitioning in continentally derived particulates. *Chemical Geology*, 214, 209–221. https://doi.org/10.1016/j.chemgeo.2004.09.003

Poulton, S. W., & Canfield, D. E. (2011). Ferruginous conditions: A dominant feature of the ocean through Earth's history. *Elements*, 7(2), 107–112. https://doi.org/10.2113/gselements.7.2.107

Poulton, S. W., & Raiswell, R. (2002). The low-temperature geochemical cycle of iron: From continental fluxes to marine sediment deposition. *American Journal of Science*, 302, 774–805. https://doi.org/10.2475/ajs.302.9.774

Raiswell, R., & Canfield, D. E. (1998). Sources of iron for pyrite formation in marine sediments. *American Journal of Science*, 298(3), 219–245. https://doi.org/10.2475/ajs.298.3.219

Raiswell, R., Hardisty, D. S., Lyons, T. W., Canfield, D. E., Owens, J. D., Planavsky, N. J., … Reinhard, C. T. (2018). The iron paleoredox proxies: A guide to the pitfalls, problems and proper practice. *American Journal of Science*, 318(5), 491–526. https://doi.org/10.2475/05.2018.03

Raven, M. R., Sessions, A. L., Fischer, W. W., & Adkins, J. F. (2016). Sedimentary pyrite δ^{34}S differs from porewater sulfide in Santa Barbara Basin: Proposed role of organic sulfur. *Geochimica et Cosmochimica Acta*, 186, 120–134. https://doi.org/10.1016/j.gca.2016.04.037

Rehkämper, M., Frank, M., Hein, J. R., & Halliday, A. (2004). Cenozoic marine geochemistry of thallium deduced from isotopic studies of ferromanganese crusts and pelagic sediments. *Earth and Planetary Science Letters*, 219, 77–91. https://doi.org/10.1016/S0012-821X(03)00703-9

Rehkämper, M., Frank, M., Hein, J. R., Porcelli, D., Halliday, A., Ingri, J., & Liebetrau, V. (2002). Thallium isotope variations in seawater and hydrogenetic, diagenetic, and hydrothermal ferromanganese deposits. *Earth and Planetary Science Letters*, 197, 65–81. https://doi.org/10.1016/S0012-821X(02)00462-4

Rehkämper, M., & Nielsen, S. G. (2004). The mass balance of dissolved thallium in the oceans. *Marine Chemistry*, 85, 125–139. https://doi.org/10.1016/j.marchem.2003.09.006

Reimers, C. E., Lange, C. B., Tabak, M., & Bernhard, J. M. (1990). Seasonal spillover and varve formation in the Santa Barbara Basin, California. *Limnology and Oceanography*, 35, 1577–1585. https://doi.org/10.4319/lo.1990.35.7.1577

Reimers, C. E., Ruttenberg, K. C., Canfield, D. E., Christiansen, M. B., & Martin, J. B. (1996). Porewater pH and authigenic phases formed in the uppermost sediments of the Santa Barbara Basin. *Geochimica et Cosmochimica Acta*, 60, 4037–4057. https://doi.org/10.1016/S0016-7037(96)00231-1

Rothman, D. H., Hayes, J. M., & Summons, R. E. (2003). Dynamics of the Neoproterozoic carbon cycle. *Proceedings of the National Academy of Sciences of the United States of America*, 100, 8124–8129. https://doi.org/10.1073/pnas.0832439100

Rue, E. L., Smith, G. J., Cutter, G. A., & Bruland, K. W. (1997). The response of trace element redox couples to suboxic conditions in the water column. *Deep Sea Research Part I: Oceanographic Research Papers*, 44, 113–134. https://doi.org/10.1016/S0967-0637(96)00088-X

Sahoo, S. K., Planavsky, N. J., Jiang, G., Kendall, B., Owens, J. D., Wang, X., … Lyons, T. W. (2016). Oceanic oxygenation events in the anoxic Ediacaran ocean. *Geobiology*, 14, 457–468. https://doi.org/10.1111/gbi.12182

Sawaki, Y., Ohno, T., Tahata, M., Komiya, T., Hirata, T., Maruyama, S., … Li, Y. (2010). The Ediacaran radiogenic Sr isotope excursion in the Doushantuo Formation in the Three Gorges area, South China. *Precambrian Research*, 176, 46–64. https://doi.org/10.1016/j.precamres.2009.10.006

Schimmelmann, A., Hendy, I. L., Dunn, L., Pak, D. K., & Lange, C. B. (2013). Revised ~2000-year chronostratigraphy of partially varved marine sediment in Santa Barbara Basin, California. *GFF*, 135, 258–264. https://doi.org/10.1080/11035897.2013.773066

Schimmelmann, A., & Kastner, M. (1993). Evolutionary changes over the last 1000 years of reduced sulfur phases and organic carbon in varved sediments of the Santa Barbara Basin, California. *Geochimica et Cosmochimica Acta*, 57, 67–78. https://doi.org/10.1016/0016-7037(93)90469-D

Scholz, F., Severmann, S., McManus, J., Noffke, A., Lomnitz, U., & Hensen, C. (2014). On the isotope composition of reactive iron in marine sediments: Redox shuttle versus early diagenesis. *Chemical Geology*, 389, 48–59. https://doi.org/10.1016/j.chemgeo.2014.09.009

Scott, C., & Lyons, T. W. (2012). Contrasting molybdenum cycling and isotopic properties in euxinic versus non-euxinic sediments and sedimentary rocks: Refining the paleoproxies. *Chemical Geology*, 324–325, 19–27. https://doi.org/10.1016/j.chemgeo.2012.05.012

Shi, W., Li, C., Luo, G., Huang, J., Algeo, T. J., Jin, C., … Cheng, M. (2018). Sulfur isotope evidence for transient marine-shelf oxidation during the Ediacaran Shuram Excursion. *Geology*, 46, 267–270. https://doi.org/10.1130/G39663.1

Sholkovitz, E. (1973). Interstitial water chemistry of the Santa Barbara Basin sediments. *Geochimica et Cosmochimica Acta*, 37, 2043–2073. https://doi.org/10.1016/0016-7037(73)90008-2

Tang, M. T., Ding, Z. J., Yao, S. Z., & Gong, Y. J. (2013). Geochemical characteristics and mineralization of Baiguoyuan Ag-V deposition in western Hubei Province. *Geological Science and Technology Information*, 32(2), 50–57. (In Chinese with English abstract)

Them, T. R., Gill, B. C., Caruthers, A. H., Gerhardt, A. M., Gröcke, D. R., Lyons, T. W., … Owens, J. D. (2018). Thallium isotopes reveal protracted anoxia during the Toarcian (Early Jurassic) associated with volcanism, carbon burial, and mass extinction. *Proceedings of the National Academy of Sciences of the United States of America*, 115, 6596–6601. https://doi.org/10.1073/pnas.1803478115

Tostevin, R., Clarkson, M. O., Gangl, S., Shields, G. A., Wood, R. A., Bowyer, F., … Stirling, C. H. (2019). Uranium isotope evidence for an expansion of anoxia in terminal Ediacaran oceans. *Earth and Planetary Science Letters*, 506, 104–112. https://doi.org/10.1016/j.epsl.2018.10.045

Tribovillard, N., Algeo, T. J., Lyons, T., & Riboulleau, A. (2006). Trace metals as paleoredox and paleoproductivity proxies: An update. *Chemical Geology*, 232(1), 12–32. https://doi.org/10.1016/j.chemgeo.2006.02.012

Turgeon, S., & Brumsack, H. J. (2006). Anoxic vs dysoxic events reflected in sediment geochemistry during the Cenomanian-Turonian Boundary Event (Cretaceous) in the Umbria-Marche Basin of central Italy. *Chemical Geology*, 234(3–4), 321–339. https://doi.org/10.1016/j.chemgeo.2006.05.008

Voegelin, A., Pfenninger, N., Petrikis, J., Majzlan, J., Plötze, M., Senn, A.-C., … Göttlicher, J. (2015). Thallium speciation and extractability in a Thallium- and Arsenic-Rich soil developed from mineralized carbonate rock. *Environmental Science & Technology*, 49, 5390–5398. https://doi.org/10.1021/acs.est.5b00629

Wang, Y., Hendy, I. L., Latimer, J. C., & Bilardello, D. (2019). Diagenesis and iron paleo-redox proxies: New perspectives from magnetic and iron speciation analyses in the Santa Barbara Basin. *Chemical Geology*, 519, 95–109. https://doi.org/10.1016/j.chemgeo.2019.04.018

Xiao, S. H., Narbonne, G. M., Zhou, C. M., Laflamme, M., Grazhdankin, D. V., Moczydlowska, M., & Cui, H. (2016). Towards an Ediacaran Time Scale: Problems, protocols, and prospects. *Episodes*, 39, 540–555. https://doi.org/10.18814/epiiugs/2016/v39i4/103886

Zhang, F., Xiao, S., Romaniello, S. J., Hardisty, D., Li, C., Melezhik, V., … Anbar, A. D. (2019). Global marine redox changes drove the rise and fall of the Ediacara biota. *Geobiology*, 17, 594–610. https://doi.org/10.1111/gbi.12359

Zhang, S., Evans, D. A. D., Li, H., Wu, H., Jiang, G., Dong, J., … Yang, T. (2013). Paleomagnetism of the late Cryogenian Nantuo Formation and paleogeographic implications for the South China Block. *Journal of Asian Earth Sciences*, 72, 164–177. https://doi.org/10.1016/j.jseaes.2012.11.022

Zhu, M., Lu, M., Zhang, J., Zhao, F., Li, G., Aihua, Y., … Zhao, M. (2013). Carbon isotope chemostratigraphy and sedimentary facies evolution of the Ediacaran Doushantuo Formation in western Hubei, South China. *Precambrian Research*, 225, 7–28. https://doi.org/10.1016/j.precamres.2011.07.019

SUPPORTING INFORMATION

Additional supporting information may be found online in the Supporting Information section.